Article

Numerically Optimized Fourier Transform-Based Beamforming Accelerated by Neural Networks

Keivan Kaboutari [ID], Abdelghafour Abraray [ID] and Stanislav Maslovski * [ID]

Instituto de Telecomunicações and Department of Electronics, Telecommunications and Informatics, University of Aveiro, 3810-193 Aveiro, Portugal; k.kaboutari@ua.pt (K.K.); abdelghafour.abraray@ua.pt (A.A.)
* Correspondence: stanislav.maslovski@ua.pt

Abstract: Conventional beamforming methods for reconfigurable reflector antennas assume full control over the amplitude and phase of the reflected field. Here, we develop a novel beamforming methodology for reflecting Programmable Metasurfaces (PMS) with capacitive memory. Although utilizing such fully reactive PMS simplifies antenna design and reduces energy consumption, the PMS reflection magnitude is unity and thus a global optimization of the reflection phases over the PMS unit cells is required in each beamforming scenario. We propose an implementation of such an optimization method rooted in the traditional Fourier transform-based beamforming and evaluate its performance. Additionally, we show that a pair of trained feed-forward neural networks (FFNN) with one input, one hidden, and one output layer can replace time-consuming global optimizations in the case of a PMS comprising 3×10 unit cells. We train the FFNNs on a dataset obtained for typical single- and dual-beam beamforming scenarios. After training, the FFNNs perform requested beamforming tasks within a fraction of second and with about the same accuracy as the original optimization algorithm. The proposed methodology may find applications in future mobile telecommunication systems that require real-time beamforming on low-end hardware. The same beamforming methodology can be also employed in short-range wireless power transfer systems.

Keywords: metasurface; Fourier transform-based beamforming; optimization; neural networks

1. Introduction

Antennas and telecommunication systems play a critical role in present-day societies. Nowadays, mobile wireless communication and data access networks are available practically everywhere around the globe. Rapid worldwide development in wireless systems has promoted a transition from the older generations to 4G+ and 5G networks. Currently, sixth-generation (6G) systems are under development to guarantee the high-speed, high-capacity, and high-quality communications dictated by the social and industrial demands of the new millennium.

Nevertheless, even with the available advanced telecommunication technologies, wireless communications continue to suffer from disturbances caused by attenuation, scattering, and diffraction of electromagnetic (EM) waves. Such unwanted phenomena occur on the signal propagation path from a transmitter (TX) to a receiver (RX). From this point of view, it is clear that achieving maximal the signal-to-noise ratio (SNR) in the propagation path between the communicating devices is essential. One of the possible methods to increase the SNR is to decrease the path loss between the TX and the RX by proactively optimizing multipath wave propagation scenarios in a dynamic environment. In particular, smart beamforming is a promising solution to guarantee wireless connectivity between the TX and RX in complex environments and achieve the best SNR.

Beamforming can be achieved with antenna systems comprising various configurations. In present-day Base Transceiver Station (BTS) systems, as well as in mobile devices, there is a tendency to employ Multiple-Input Multiple-Output (MIMO) antennas to achieve

channel diversity [1–6]. Usually, elementary antennas in such MIMO systems (or antenna arrays) can be realized with inexpensive Printed Circuit Board (PCB)-based techniques (e.g., microstrip or coplanar) and can be used for transmitting and receiving all kinds of information [7–14].

Several methods exist to create and steer antenna array beams, ranging from the classical Butler matrix approach to the actively developed smart and reconfigurable antenna concepts. In 1961, Butler and Lowe proposed their methodology for passive beamforming [15,16]; this was a development of an earlier work by Blass [17]. Butler matrices are commonly used for feeding various antenna arrays with wide angular coverage [18]. A typical system may comprise an $N \times N$ matrix of fixed-value phase shifters and hybrid couplers, where N is a power of 2. An antenna array equipped with such a matrix may have N input ports (the beam ports) to which power is applied and N output ports (the element ports) to which N antennas are connected. The Butler matrix provides power to the elements with a progressive phase difference between the elements such that the antenna main beam points in a selected direction. The beam direction is controlled by switching the input power between the beam ports. More than one beam or even all N of them can be activated simultaneously.

Since Butler's matrix can be realized with microstrip lines, it is a cost-effective solution for achieving directional beam control without the need to deploy an array of expensive active phase shifters. Hence, its fabrication cost can be just a small fraction of the cost of a full-fledged antenna array feeding network. However, its relative hardware simplicity comes at the cost of having to deal with a bulky structure and a fixed set of predefined beam directions. Indeed, Figure 1 depicts a Butler matrix-based beamforming system [18] comprising eight input ports and eight antenna ports. This system is able to produce up to eight fixed beams with inclinations in the range of about $\pm 55°$. Per antenna element, this design requires one input feed, one phase shifter, and one and a half hybrid couplers. In typical designs, the 90-degree hybrid couplers are formed by four segments of quarter-wavelength microstrip lines. Therefore, at the operating frequency of 5 GHz, each coupler may occupy an area of about 1 cm^2. Moreover, additional phase compensation lines are required to obtain the necessary phase shifts within the Butler matrix [18]. Thus, integrating the Butler network on the same PCB with antenna array elements may impose limits on the element placement density, especially when the number of input ports approaches the number of elements.
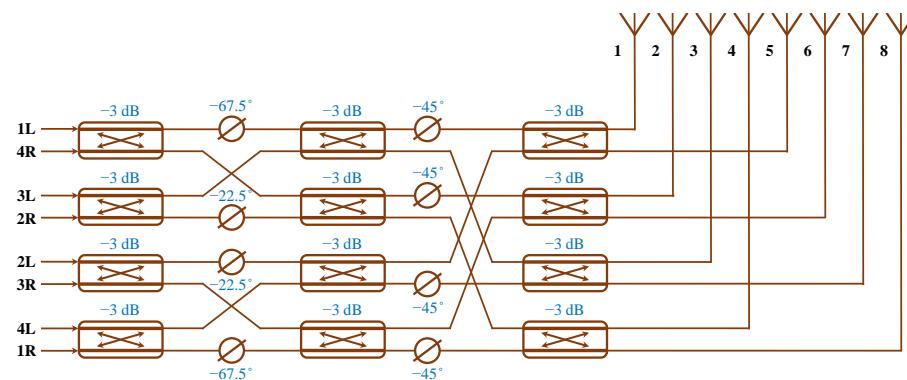

Figure 1. Schematic of an 8×8 Butler matrix comprising 8 phase shifters and 12 hybrid couplers [18]. The eight input ports are denoted as 1L–4L and 1R–4R. The eight output ports are marked as 1–8.

On the other hand, among the more expensive actively controlled antenna systems, there are electronically/digitally controlled phased array antennas of various kinds, which can be assembled in linear, planar, or conformal configurations [19–23]. Such antennas can provide flexible electronic beam steering in less than milliseconds, eliminating any need for mechanical steering. They may produce multiple beams simultaneously and perform multifunction operations with independent beam control. Unlike passive phased array antennas, the active ones can also simultaneously emit and receive multiple radio signals

at multiple frequencies in different directions, which is used for surveillance and tracking in radar applications. Although highly reconfigurable, these devices may also suffer from drawbacks such as limited coverage in both the azimuth and elevation planes (with a linear array, beam deflection is only possible in a single plane). Moreover, active phased array networks are very complex and require elements with sophisticated electronic controls that are available at a high cost, although their frequency agility can be limited [24–26].

During the last decade, an alternative concept that combines the advantages of the passive systems (e.g., low energy consumption and cost) and the active systems (e.g., flexible reconfigurability) has emerged: the concept of Programmable Metasurfaces (PMS) [27–29]. In recent years, PMS have been under active investigation. In particular, it has been demonstrated that PMS or Reflecting Intelligent Surfaces (RIS) can be used to adjust channel propagation conditions [30,31]. In PMS-enhanced systems, the TX and RX antenna radiation patterns can be dynamically controlled to facilitate wireless communications in varying propagation environments.

Indeed, it is known that microwave or optical metasurfaces (MS) can alter the propagation direction of the EM waves by creating phase gradients along their surface [32,33]. In particular, the PMS may act as mirrors in reconfigurable reflector antennas. In such antennas, versatile beamforming can be achieved by controlling both the phase and amplitude of wavefronts reflected from an MS [34–37]. However, in order to freely control the reflection amplitude at MS unit cells, active components (such as amplifiers or impedance inverters, etc.) may be needed. In this case, the effective surface impedance of the MS becomes complex. The sign of the real part of the surface impedance determines if there is attenuation or amplification of the signal locally reflected at that point. On the other hand, if the reflection amplitude control is not required, then the MS can be completely passive (reactive). Some form of amplitude control can be achieved even in purely reactive MS, e.g., by an approach that one may call "surface mode engineering", when the surface mode resonances supported by the MS are tuned in a way to redistribute the reactive power (i.e., power of local oscillations) along the MS.

When comparing the PMS-based systems with the Butler matrix-based ones, one may notice that, per unit cell, the PMS-based systems typically need just a few Surface-Mounted (SMT) components with dimensions on the order of 1 mm or less, whilst Butler matrices require a network of hybrid couplers and phase shifters realized with microstrip lines whose dimensions are mandated by the operation wavelength and the power handling requirements. Therefore, in PMS-based systems, the unit cell size is not as restricted by the size of the auxiliary (i.e., control) components. At microwave frequencies, this enables realizations with unit cell dimensions significantly smaller than the wavelength (e.g., from 1/10 to 1/5 of the wavelength). Having smaller unit cells is important in complex beamforming scenarios as it improves accuracy of the aperture field representation.

For example, a single-layer passive MS is proposed in [38,39] to control the phase and amplitude of the EM field in an antenna aperture plane. The MS is intended to transform a cylindrical incident wave into a directive far-field pattern with the main beam inclined by 30° with respect to the MS normal. A fully reactive MS has been attained by applying an optimization algorithm to generate the desired near and far fields. In their method, the MS surface impedance as a function of location is initially obtained from the desired aperture field distribution. However, the impedance found in this way is complex with the real part changing sign at different locations on the MS. Next, the real part is made negligible by applying a global optimization to the surface impedance distribution with a goal to obtain a merely reactive MS, while keeping the same far-field radiation pattern. In a nutshell, such optimization adjusts the MS surface reactance at different locations in order to generate a proper evanescent wave spectrum near the MS and maintain the surface waves needed to redistribute the reactive power on the MS and produce the desired far-field pattern.

Metaheuristic optimization and Artificial Intelligence (AI) algorithms such as Particle Swarm Optimization (PSO), Genetic Algorithms (GA), and various Artificial Neural Network (ANN) algorithms have been employed in the design of metasurfaces for various

applications [40–42]. In particular, Machine Learning (ML) and ANN approaches have gained massive attention in recent years. Indeed, ML concepts have already helped to solve many practical problems and demonstrated promising results in optimization, identification, and prediction problems in systems that exhibit nonlinear, dynamic, and complex behaviors. We believe that Feed-Forward Neural Networks (FFNN) can open new research venues in beamforming and highly efficient wave manipulation [42–44], because FFNN are able to model complex nonlinear systems with only a limited set of input parameters after suitable training is performed.

In this article, we supersede the traditional Fourier transform-based (FT-based) beamforming methods that rely on the well-known link between the far-field pattern and the antenna aperture field by proposing a Fourier transform-based beamforming enhanced with a pretrained FFNN. Indeed, in many works on reconfigurable beamforming MS, it is assumed that the required phase distribution on the MS aperture is determined by the Fourier transform of the far-field radiation pattern. However, additional steps are necessary in order to increase beamforming accuracy. Preliminary concepts of how FFNN could be used to implement these steps were introduced in [45,46].

As was discussed earlier, although simultaneous amplitude and phase control of the aperture field is, in principle, possible with active PMS, it leads to increased complexity and fabrication costs. As a measure of complexity, one can use the number of controllable elements and other electronic components per unit cell in a given design. For example, the RIS described in [47] uses only two pin diodes per unit cell to adjust the reflection phase. However, it requires complicated electronics with many digital Integrated Circuits (ICs) to realize reconfigurability. As is seen in Figure 3 from [47], the number of ICs at the back side of the RIS is greater than the number of unit cells. As was reported in [47], the fabricated 10×10 cm^2 RIS sample consumed 8 W of dc power. In [48], which describes a non-reciprocal transmitting PMS ("meta-prism"), each unit cell comprises two antenna elements on the opposite sides of the PMS, two variable gain amplifiers, and an electronically tunable phase shifter. Although such a "meta-prism" allows for independent control of the signal amplitude and phase, such functionality was achieved with the cost of increased complexity.

Conventional beamforming methods assume full control over the amplitude and phase distributions over the antenna aperture. On the other hand, our fully reactive PMS design [28,46] achieves full 360° reflection phase control, albeit with a fixed reflection magnitude. On the hardware level, this allows us to eliminate active components and reduce the PMS cost and complexity; however, it complicates the relation between the desired radiation pattern and the aperture phase distribution. Therefore, in the beamforming methodology that is developed next, we apply optimization methods (e.g., Nelder–Mead, PSO, pattern search [49–51]) to fine-tune the initial Fourier transform-based aperture phases and attain the desired far-field pattern.

With the optimization framework developed in this paper, we define and minimize a constrained nonlinear multivariable cost function that encodes the desired multi-beam radiation pattern. The required aperture phase distribution is obtained iteratively after many rounds of cost function minimization steps. Finally, we apply AI methods such as trained ANN to sidestep the time-consuming numerical optimization techniques and pave the way to real-time beamforming on inexpensive hardware. Figure 2 shows a conceptual diagram of our methodology. Here, we use FFNN to predict phase distributions and control voltages for an electronically controlled PMS that we have designed earlier [28,29]. Two different types of ANN are proposed based on the FFNN model. The first trained ANN, Beamforming Neural Network (BFNN), relates the desired main beam characteristics to the required phase distribution over the MS. Consequently, the second ANN formed by Controlling Neural Network (CTRLNN) blocks, relates the phase distribution to the necessary control voltages applied to the cells of the MS. We train the FFNN on a dataset obtained for typical beamforming scenarios by using the optimization methodology outlined above. After training, the FFNN is able to perform beamforming tasks with about the

same accuracy as the original optimization algorithm. Because trained ANNs can produce results in a much shorter time [40] compared to time-consuming global optimizations, this approach is beneficial for real-time beamforming.
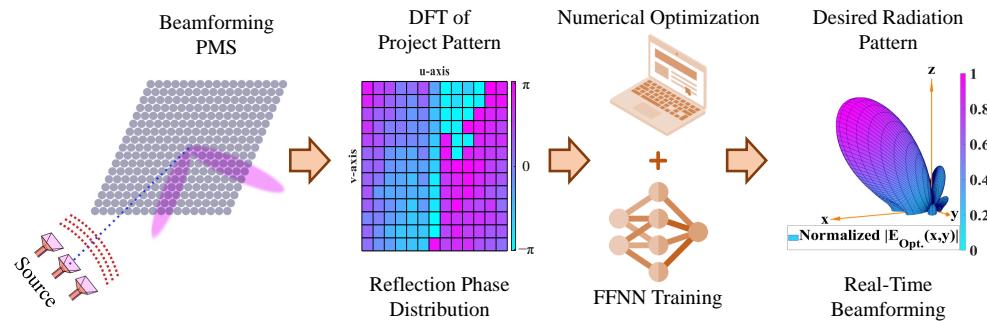

Figure 2. Conceptual diagram of numerically optimized FT-based beamforming accelerated by FFNN.

2. FT-Based Beamforming Methodology for Reflecting PMS

We consider a PMS-based beamforming antenna with separately controllable $N \times M$ reflecting elements, which are the unit cells of the PMS. Here, N and M are the numbers of rows and columns of the PMS elements, respectively. Moreover, we suppose that the antenna operates at either $f_1 = 5$ GHz or $f_2 = 10$ GHz. These two frequencies will be used to conduct simulations and numerical studies of the proposed PMS and the beamforming methodology. The period of the PMS structure, which is also the distance between the element centers along x and y directions, is $d = 6.8$ mm, which is about $\lambda_1/9 = \lambda_2/4.5$, where λ_1 and λ_2 are the free-space wavelengths at the two considered frequencies. A feed antenna with low directivity illuminates the PMS, Figure 3a, and the far-field radiation pattern is formed after the PMS reflects the illuminating field, Figure 3b. In Figure 3a, R_f is the distance from the feed antenna to the PMS plane (the focal distance) and R_{mn} (denoted as $R(m, n)$ in the figure) is the radial distance from the same antenna to the (m, n)-th element of the PMS, Equation (1):

$$R_{mn} = \sqrt{R_f^2 + \left(\left(m - \frac{M-1}{2} \right)^2 + \left(n - \frac{N-1}{2} \right)^2 \right) d^2}. \tag{1}$$
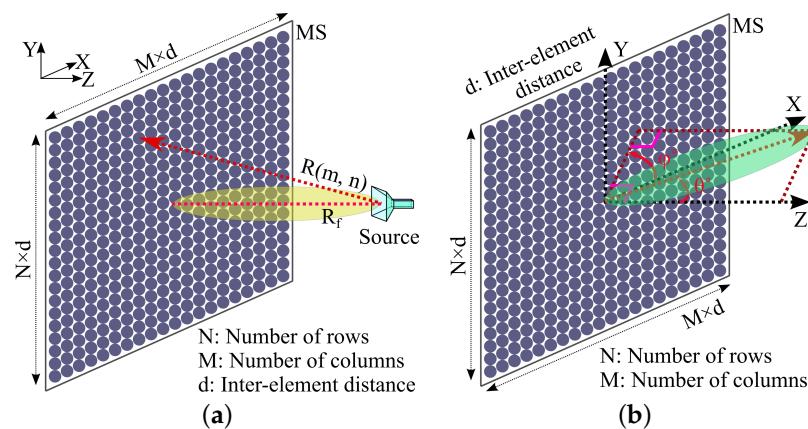

Figure 3. Reconfigurable MS-based reflect array antenna. (**a**) Illuminating a reconfigurable MS-based reflect array antenna by a source antenna. (**b**) Reflected beam at the prescribed direction produced by a reconfigurable MS-based reflect array antenna.

Radiation patterns are typically expressed in the spherical coordinate system. However, for us it will be more convenient to specify the antenna patterns in the (u, v)-space with the orthogonal coordinates u and v that are related to the spherical angles θ and φ

as follows: $u = k_0 d \sin\theta \cos\varphi$, $v = k_0 d \sin\theta \sin\varphi$, where k_0 is the free-space wavenumber, which equals either $2\pi/\lambda_1$ or $2\pi/\lambda_2$, according to the selected operating wavelength.

It makes sense to consider a set of aperture patterns, $F_a(u,v)$, represented by superpositions of sinc -like terms, where $\text{sinc}\, x = \frac{\sin \pi x}{\pi x}$, Equation (2),

$$F_a(u,v) = \sum_{i=1}^{L} a_i \, \text{sinc}\, \frac{s_x(u - u_{0,i})}{2\pi} \, \text{sinc}\, \frac{s_y(v - v_{0,i})}{2\pi}, \tag{2}$$

as these are good approximations for the elementary patterns of a rectangular aperture of $s_x d$ by $s_y d$ size. Here, s_x and s_y are aperture dimensions (along the x- and y-axes) normalized to the PMS period d. In this study, $s_x = M$ and $s_y = N$. Increasing or decreasing the aperture sizes makes the beams narrower or wider, respectively. The amplitude factors a_i are set to unity in this study for simplicity. However, as is explained in Section 3.2, each beam can have a separate scale factor assigned to it during the aperture phase optimization process. Physically, $F_a(u,v)$ represents an approximation of the radiation pattern of a dense array of isotropic emitters. The pattern has L main beams pointing at the directions in the (u,v)-space defined by vectors $(u_{0,i}, v_{0,i}) = (k_0 d \sin\theta_i \cos\varphi_i, k_0 d \sin\theta_i \sin\varphi_i)$, where θ_i and φ_i are the spherical angles corresponding to the i-th beam direction.

Due to vectorial nature of the EM fields, the radiation pattern of a reflecting PMS must include a correction that takes into account the direction of the surface electric currents induced on the PMS. This is determined by the incident electric field polarization produced by the feed antenna. In what follows, we assume that the incident electric field is linearly polarized along the x-axis, and, therefore, the induced currents on the PMS are also dominantly x-polarized. It can be shown that in this case we must define a set of polarization-corrected project patterns, $F(u,v)$, as

$$F(u,v) = \sqrt{1 - \left(\frac{u}{k_0 d}\right)^2} F_a(u,v). \tag{3}$$

Note that by using the terminology of phased array antennas, $F_a(u,v)$ can be regarded as the array factor and the square root term in front of it can be regarded as the radiation pattern of a single element of the array.

Instead of using $F(u,v)$ as a continuous function of two variables, let us take discrete samples of it, F_{kl}, obtained as follows:

$$F_{kl} = F\left(\frac{2\pi(k - \frac{M-1}{2})}{M - 1}, \frac{2\pi(l - \frac{N-1}{2})}{N - 1}\right). \tag{4}$$

Here, the indices $k \in [0; M-1]$ and $l \in [0; N-1]$ label the (k,l)-th sample of the radiation pattern in the (u,v)-space. Consequently, the necessary amplitude and phase distribution on the PMS aperture can be found by applying a discrete Fourier transform to the discretized project pattern, since, as is well known, the far-field radiation pattern of a rectangular aperture in such coordinates is equivalent to the Fourier transform of the aperture wave field. As was mentioned in the introduction, we neglect the amplitude of the Fourier-transformed pattern and just consider its phase.

In addition to the aperture phase distribution dictated by the Fourier-transformed project pattern, in order to find the actual aperture field phase, Φ_{mn}, at a given PMS element, we must compensate for the varying delay acquired by the incident field when propagating from the feed antenna to the given element. Hence, by using the two-dimensional discrete Fourier transform, the aperture phase can be expressed as in Equation (5):

$$\Phi_{mn} = k_0 R_{mn} + \angle \sum_{k=0}^{M-1} \sum_{l=0}^{N-1} F_{kl} e^{-2\pi i \left(\frac{(m - \frac{M-1}{2})(k - \frac{M-1}{2})}{M} + \frac{(n - \frac{N-1}{2})(l - \frac{N-1}{2})}{N}\right)}, \tag{5}$$

where we have used the notation $\angle z \equiv \arg z$. Next, the phase Φ_{mn} is used to obtain the complex phasor $\Omega_{mn} = a_{mn}e^{i\Phi_{mn}}$, with the amplitude factor a_{mn} set to unity for all unit cells.

Finally, the actual far-field electric field pattern (here we are interested in unnormalized magnitude pattern) produced by the PMS is expressed as follows:

$$|\mathbf{E}(u,v)| \propto \sqrt{1 - \left(\frac{u}{k_0 d}\right)^2} \sum_{m=0}^{M-1}\sum_{n=0}^{N-1} \frac{\Omega_{mn}e^{i\left(m-\frac{M-1}{2}\right)u+i\left(n-\frac{N-1}{2}\right)v-ik_0 R_{mn}}}{R_{mn}}. \tag{6}$$

This expression includes the spherical wave amplitude factor $1/R_{mn}$ to account for the incident field propagation decay.

When the actual pattern given by Equation (6) is compared with the project pattern, Equation (3), we have noticed that, despite fixing the magnitude to unity and keeping only the aperture phase information, the project pattern is accurately regenerated with acceptable sidelobe levels for some single-beam cases. However, in many other cases, the reconstructed pattern has multiple sidelobes with unacceptably high levels. Moreover, a shift may occur in the direction of the main beam.

For instance, the project pattern and the reconstructed electric field pattern in the (u, v)-space created by a 10×3 PMS with 50 cm focal distance that operates at 5 GHz and produces a single-beam directed at $(u_{0,1}, v_{0,1}) = (-0.47, -0.41)$ are depicted in Figure 4a,b. In these figures, the green circle represents the beam visibility range $\sqrt{u^2 + v^2} \leq k_0 d$. The red oval depicts the protected area range, the meaning of which will be explained in Section 3.1. One can see that in this case the reconstructed main beam is wider than the project pattern main beam. In addition, the main beam is displaced from the original position and there are strong secondary maxima outside the visibility range.

The situation becomes more complex for multi-beam radiation patterns, in which the direction shift and the sidelobe levels may become even larger. For example, the project pattern and the reconstructed electric field pattern created by the same PMS operating at 10 GHz with two main beams directed at $(u_{0,1}, v_{0,1}) = (0.51, 0.51)$ and $(u_{0,2}, v_{0,2}) = (-0.51, -0.51)$ are shown in Figure 4c,d. These figures demonstrate that the two main beams in the reconstructed pattern merge under these conditions. This is even better seen in Figure 5a,b, which depict the patterns as surfaces in the real three-dimensional (3D) space (x, y, z). In this representation, which is limited to the visible range only, the far-field magnitude in a given direction in the 3D space is proportional to the distance from the origin to the corresponding point on the plot surface.
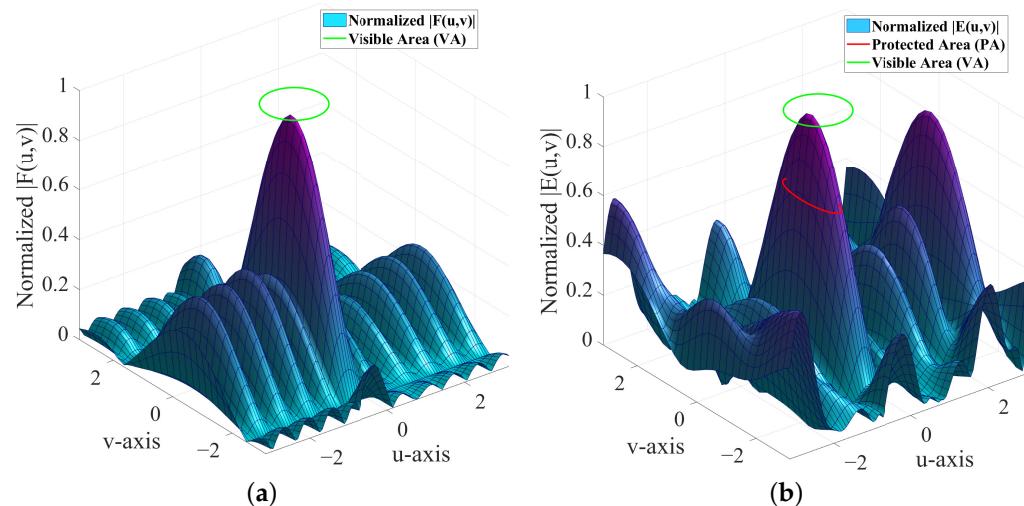

Figure 4. *Cont.*
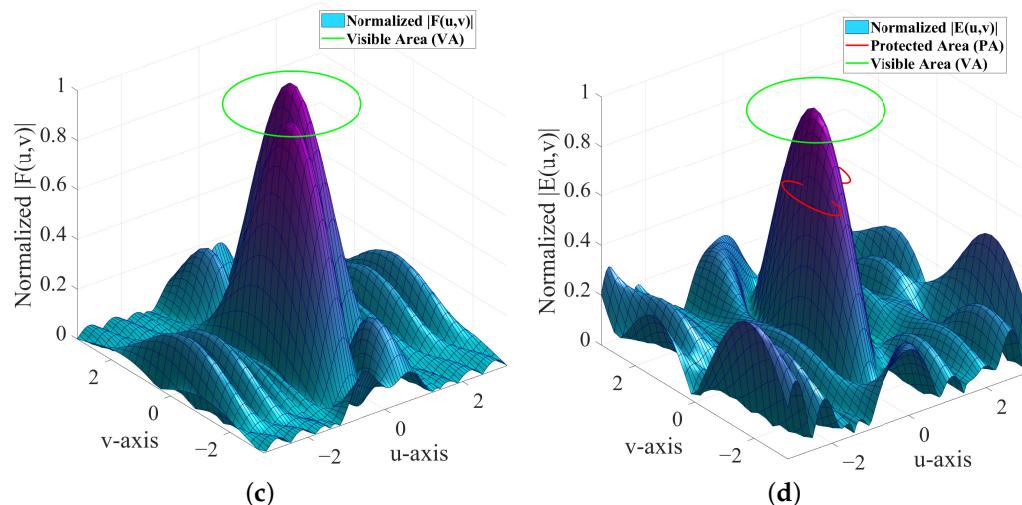
Figure 4. Normalized project pattern and reconstructed electric field pattern for the single-beam (**a**,**b**) and the dual-beam (**c**,**d**) cases in the (u, v)-space, as produced by a 10×3 PMS. (**a**) Normalized project pattern at 5 GHz, single-beam at $(\theta_{0_1}, \varphi_{0_1}) = (60.2°, 221.1°)$. (**b**) Normalized reconstructed electric field pattern at 5 GHz, with $(\theta_{0_1}, \varphi_{0_1}) = (60.2°, 221.1°)$. (**c**) Normalized project pattern at 10 GHz, dual-beam at $(\theta_{0_1}, \varphi_{0_1}) = (30°, 45°)$ and $(\theta_{0_2}, \varphi_{0_2}) = (30°, 225°)$. (**d**) Normalized reconstructed electric field pattern at 10 GHz, with $(\theta_{0_1}, \varphi_{0_1}) = (30°, 45°)$ and $(\theta_{0_2}, \varphi_{0_2}) = (30°, 225°)$.
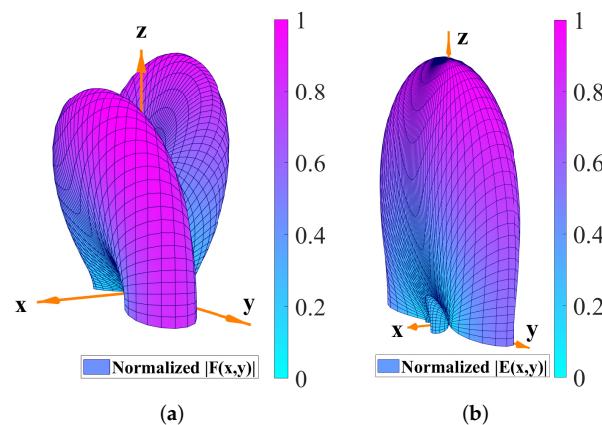

Figure 5. Normalized project pattern and reconstructed electric field pattern at 10 GHz for the dual-beam case in the spherical coordinates, as generated by a 10×3 PMS. (**a**) Normalized project pattern, $(\theta_{0_1}, \varphi_{0_1}) = (30°, 45°)$ and $(\theta_{0_2}, \varphi_{0_2}) = (30°, 225°)$. (**b**) Normalized reconstructed electric field pattern, $(\theta_{0_1}, \varphi_{0_1}) = (30°, 45°)$ and $(\theta_{0_2}, \varphi_{0_2}) = (30°, 225°)$.

Consequently, we may conclude that using the FT-based beamforming alone may lead to large inaccuracies in the reproduced radiation patterns. Therefore, applying an optimization to the Fourier transform-based initial phases is necessary in order to suppress unwanted sidelobes and achieve a reasonable accuracy. However, we have to note here that involving optimization algorithms is time-consuming, which in many cases forbids real-time beamforming, especially on inexpensive hardware. Therefore, in Section 5 we will discuss how the optimized phase data can be used to train an ANN and how the trained ANN can be utilized to achieve beamforming in real time.

3. Algorithms for Phase Distribution Optimization

As mentioned above, the sidelobe levels increase when considering the phase information and neglecting the magnitude information on the PMS aperture. Indeed, the considered PMS only controls the phase of the reflected field and the magnitude information of the aperture field is lost. Therefore, the bare FT-based beamforming method

needs to be complemented by a numerical optimization step that adjusts the aperture phase distribution in order to overcome this shortcoming.

3.1. Clustering of (u, v)-Space during Optimization

To produce an efficient algorithm for optimization of the phase distribution, one should create a suitable cost function related to the reconstructed electric field pattern. Then, the desired pattern characteristics can be improved by manipulating the phase distribution over the PMS aperture. In particular, the cost function should be defined in such a way that the optimization leads to an increase in the main beam's amplitude and suppression of the sidelobes. For this goal, the whole area in (u, v)-space is clustered into three sections, as explained next.

According to the operating frequency and the PMS physical size, there are regions of the (u, v)-space that correspond to the propagating waves, for which the normalized propagation constant $k_z d \equiv \sqrt{(k_0 d)^2 - u^2 - v^2}$ is purely real, and to the evanescent waves with imaginary propagation constant along the z-axis. We call the region that corresponds to the evanescent waves the Invisible Area (IA). This region does not affect the main lobe or the sidelobes located in the physical region of propagating waves.

Correspondingly, the Visible Area (VA) corresponds to the part of the (u, v)-space that is characterized with the real-valued propagation constants, and any changes to the phase distribution that affect this area will affect the main lobe and the sidelobes. It is evident from the above that the VA is a disk centered at the point $(0, 0)$ in the (u, v)-space with the radius equal to $k_0 d$.

The third cluster that we consider is formed by the oval-shaped Protected Areas (PAs) defined around the main beams. The primary purpose of specifying PAs is to avoid a decrease in the main beam magnitude during the optimization process due to the phase distribution manipulation over the MS. The centers of the PAs are positioned at the locations of the main beams, $(u_{0,i}, v_{0,i})$, in the (u, v)-space. In some situations, PAs intersect with the IA, which depends on the beams' direction/location and the selected PAs radii. However, locating these areas inside the visible area is more beneficial and helps to obtain the highest possible PMS performance.

The radii of the PAs are determined by solving Equations (7) and (8) and multiplying the results by $2\pi/s_x$ and $2\pi/s_y$, respectively:

$$\text{sinc}\,(u) = 1/p \Rightarrow \text{root}\, u' > 0 \xrightarrow{scaling} u'' = \frac{2\pi u'}{s_x}, \tag{7}$$

$$\text{sinc}\,(v) = 1/q \Rightarrow \text{root}\, v' > 0 \xrightarrow{scaling} v'' = \frac{2\pi v'}{s_y}. \tag{8}$$

Therefore, each PA corresponds to the interior part of an ellipse as given by

$$\frac{(u - u_{0,i})^2}{u''^2} + \frac{(v - v_{0,i})^2}{v''^2} = 1.$$

Increasing or decreasing the values of the parameters $1 < p \leq 4$, $1 < q \leq 4$ increases or decreases the radii of PAs. Therefore, to cover at least the Half-Power Beam Width (HPBW) of the main beams, the values of p and q should be adjusted considering the operating frequency, the number of MS elements, etc.

Consequently, every point (u, v) that satisfies the following inequality [Equation (9)] belongs to the corresponding PA:

$$\text{PA}_i: \quad \forall (u, v), \quad \frac{(u - u_{0,i})^2}{u''^2} + \frac{(v - v_{0,i})^2}{v''^2} - 1 < 0. \tag{9}$$

3.2. Definition of Cost Function and Sampling Method

The optimization process strongly depends on the selection of the cost function expressed in terms of the electric field radiation pattern, $|\mathbf{E}(u,v)|$. Due to the aforementioned reasons, the cost function should include two terms to divide the radiation pattern domain into two regions. The first term should cover the PAs. The second term covers the domains that do not fit into PAs, i.e., the Unprotected Area (UA). Therefore, the cost function Ψ can be defined as follows:

$$\Psi = C_1 \Psi_{PA} + C_2 \Psi_{UA}. \tag{10}$$

The optimization goal should be defined so as to minimize the cost function and acquire the desired pattern. Reaching this goal depends on the coefficients $C_1 > 0$ and $C_2 > 0$ in Equation (10), which are weights that specify the importance of each region and its influence on the cost function.

In a practical realization of the optimization algorithm, samples are taken from the electric field pattern to find the radiated power magnitude at every point in the (u,v)-space. The cost function values for each area are calculated using the acquired power samples, as in Equations (11) and (12):

$$\Psi_{UA} = \sum_{k=1}^{p} |\mathbf{E}(u_k, v_k)|^2, \tag{11}$$

where k and p are the index and the number of sample points outside the PA, respectively. Here, $|\mathbf{E}(u_k, v_k)|$ is the PMS-generated far-zone electric field taken at the k-th sample point outside the PA [Equation (6)]. On the other hand, within the PA,

$$\Psi_{PA} = \sum_{i=1}^{L} \sum_{j=1}^{q} \Big| |\mathbf{E}(u_{ij}, v_{ij})| - \alpha_i \beta |F(u_{ij}, v_{ij})| \Big|^t, \tag{12}$$

where the index i iterates over L main beams and j and q are the index and the number of sample points inside the i-th protected area, respectively. Here, $|\mathbf{E}(u_{ij}, v_{ij})|$ is the far-zone electric field updated at every cost function evaluation, and $|F(u_{ij}, v_{ij})|$ is the magnitude of the project pattern defined by Equation (3). Both quantities are evaluated at the points (u_{ij}, v_{ij}) inside the i-th protected area. In total, $p + L \times q$ points are sampled to evaluate the final cost function, Equation (10). In Figure 6, examples of the sampling of $|\mathbf{E}(u,v)|$ are shown for a couple of considered scenarios.
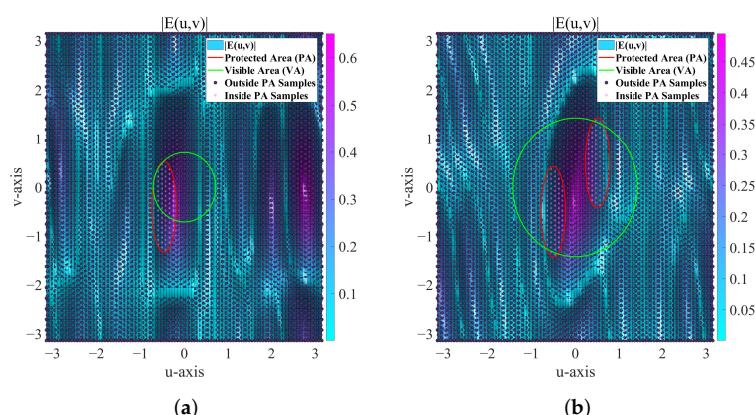

(a)   (b)

Figure 6. Sampling of the reconstructed electric field pattern for the single-beam and dual-beam cases corresponding to a 10×3 PMS. The green circles delineate the VAs and the red ovals mark the PAs. The background colors represent $|\mathbf{E}(u,v)|$ values before optimization. (**a**) Single-beam scenario for $(\theta_{0_1}, \varphi_{0_1}) = (60.2°, 221.1°)$. (**b**) Dual-beam scenario for $(\theta_{0_1}, \varphi_{0_1}) = (60.2°, 45°)$ and $(\theta_{0_2}, \varphi_{0_2}) = (30°, 225°)$.

Furthermore, in Equation (12), $\alpha_i > 0$ is a controlling factor that can manipulate the magnitude of a specific main beam in multi-beam scenarios and serve as a scale factor per each beam. Additionally, the quantity $\beta > 0$ must be selected properly to adjust for the difference in scales of the values given by Equations (3) and (6). The gain in the main beams should increase after applying phase distribution optimization due to the law of energy conservation because such optimization leads to a decrease in the overall sidelobe level. This allows the algorithm to properly suppress the sidelobes and increase the main beams' gain at the same time. Finally, the exponent $t > 0$ can be used to adjust the convergence rate of the optimization algorithm.

3.3. Applying Filtering on Protected Areas

As mentioned before, the (u, v) domain is split into two main areas: VA and IA, as mandated by the PMS structure dimensions and operating frequency. The regions inside the IA have no immediate effect on the main beams. In contrast, the VA region has a pronounced effect and is subdivided further into the protected and unprotected areas (PAs and UA). One may argue that the significance of points inside PAs decreases when moving away from the PAs centers. To account for this, one can apply a Gaussian filter centered at $(u_{0,i}, v_{0,i})$ with the magnitude of unity and the standard deviation $\sigma = k_0 d$. Thus, the main beams can be multiplied by such filter, Equation (13), before constructing the cost function to speed up the optimization process:

$$G_i(u, v) = e^{-\frac{(u-u_{0,i})^2 + (v-v_{0,i})^2}{2\sigma^2}}. \tag{13}$$

where i denotes the beam index. When using such Gaussian filtering, a common multiplier $G_i(u_{ij}, v_{ij})$ is included into Equation (12) under the double summation sign.

3.4. Evaluating Optimization Methods

In this section, we discuss how optimization algorithms could be implemented in order to decrease the sidelobe levels in a beamforming system equipped with the reflecting PMS introduced previously. For this purpose, several optimization algorithms have been employed to conduct simulations and control the phase distribution over the MS to diminish the sidelobe levels. By decreasing sidelobe levels, the gain of the main beams should increase due to the law of energy conservation. Optimization algorithms such as Nelder–Mead, PSO, as well as other methods to a find a minimum of (possibly constrained) nonlinear multivariable function (e.g., `patternsearch`, `fmincon` from MATLAB) have been tested.

We have discovered that straightforward algorithms such as Nelder–Mead could not converge to a stable value of the cost function, and the generated results oscillated around the initial values. In contrast, the PSO algorithm produced better results when starting optimization process with the initial phase distribution obtained by the Fourier transform method. We observed that in most cases this algorithm gradually converges to a stable minimal value of the cost function.

We have observed that optimization using a pattern search algorithm `patternsearch` also converged, but rather slowly. Finally, an optimization method that searches for a minimum of a constrained nonlinear multivariable function, `fmincon`, was selected as producing the most reliable results. By default, this optimization method uses an interior-point algorithm to reduce the cost function. The employed algorithm converges to the final result faster than other tested algorithms when starting from the initial phase distributions obtained from the Fourier transform. Moreover, this method has the ability to be combined with other optimization algorithms to obtain even faster convergence. Some results illustrating the convergence rate and the achievable minimal cost function value are presented in Figure 7.
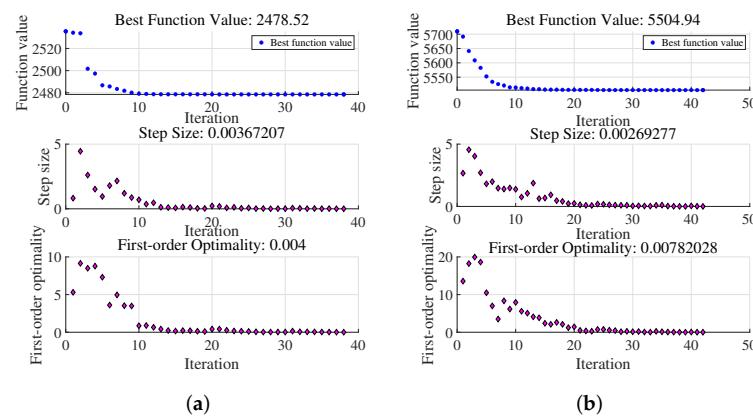
Figure 7. Evaluation of optimization process performance for single-beam and dual-beam patterns generated by a 10×3 PMS. The plots show evolution of the cost function values, step size, and optimality vs. number of iterations. (**a**) Single-beam scenario. (**b**) Dual-beam scenario.

4. Optimization Results for Single-Beam and Dual-Beam Cases

To suppress sidelobes and adjust the main beams to realize the target pattern with a higher accuracy, an optimization algorithm, fmincom, which finds a minimum of constrained nonlinear multivariable function, was employed. When evaluating the cost function from Section 3.2, the parameters C_1, C_2, and t were set to 10, 1, and 1.3, respectively, in order to increase the convergence rate and enhance the optimization results. These values have been obtained by a "trial and error" method by running several test optimizations and evaluating their outputs.

The coefficients α_i have been set to $1/\max |F(u,v)|_{PA}$ within each PA, since our objective is to recover all beams with the same magnitude. The coefficient β was determined based on the estimated attainable maximum of $|\mathbf{E}(u,v)|$ within the VA: $\beta \approx \max |\mathbf{E}(u,v)|_{VA}$. This value can be determined only after a few trial optimizations. As an initial guess, one can use the value obtained with unoptimized electric field pattern. The optimal value of β is larger than that. In some cases that we have considered, the optimal value was found to be about five times greater than the initial guess value.

To test the proposed optimization approach, we have performed a number of numerical simulations. In Figure 8, we show a couple of example phase distributions over the PMS before and after applying the optimization process for single- and dual-beam scenarios for a PMS composed of 10×3 unit cells. Despite the fact that the initial phase distributions [Figure 8a,c] show irregular patterns, the optimization process recovers the expected phase gradients over the PMS surface in the two considered scenarios [Figure 8b,d].
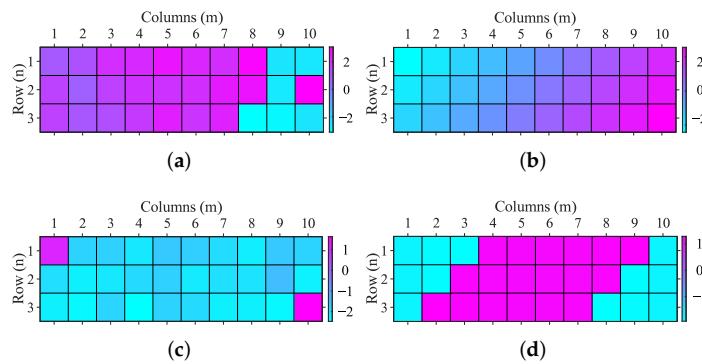

Figure 8. Phase distributions over a 10×3 PMS in the single-beam and dual-beam scenarios. (**a**) Single-beam scenario before applying optimization. (**b**) Single-beam scenario after applying optimization. (**c**) Dual-beam scenario before applying optimization. (**d**) Dual-beam scenario after applying optimization.

Figure 9 shows the optimized normalized electric field pattern in the same two scenarios, depicted in the (u, v)-space [Figure 9a,c] and in the spherical coordinates in 3D space corresponding to the VA [Figure 9b,d]. In the single-beam scenario, tilting of the main beam in the xz-plane with respect to the normal to the PMS (the z-axis) is clearly visible. Inclination of the beam in yz-plane is also recognizable; however, because the PMS size along the y direction is smaller, the beam directivity in this plane is poor. In the realized dual-beam scenario shown in Figure 9b,d, the two beams have symmetric inclinations with respect to the PMS normal. The optimization process was able to recover the two main beams, despite the fact that the initial aperture phase data, if used directly, would result in a merged beam like that shown in Figure 5b.
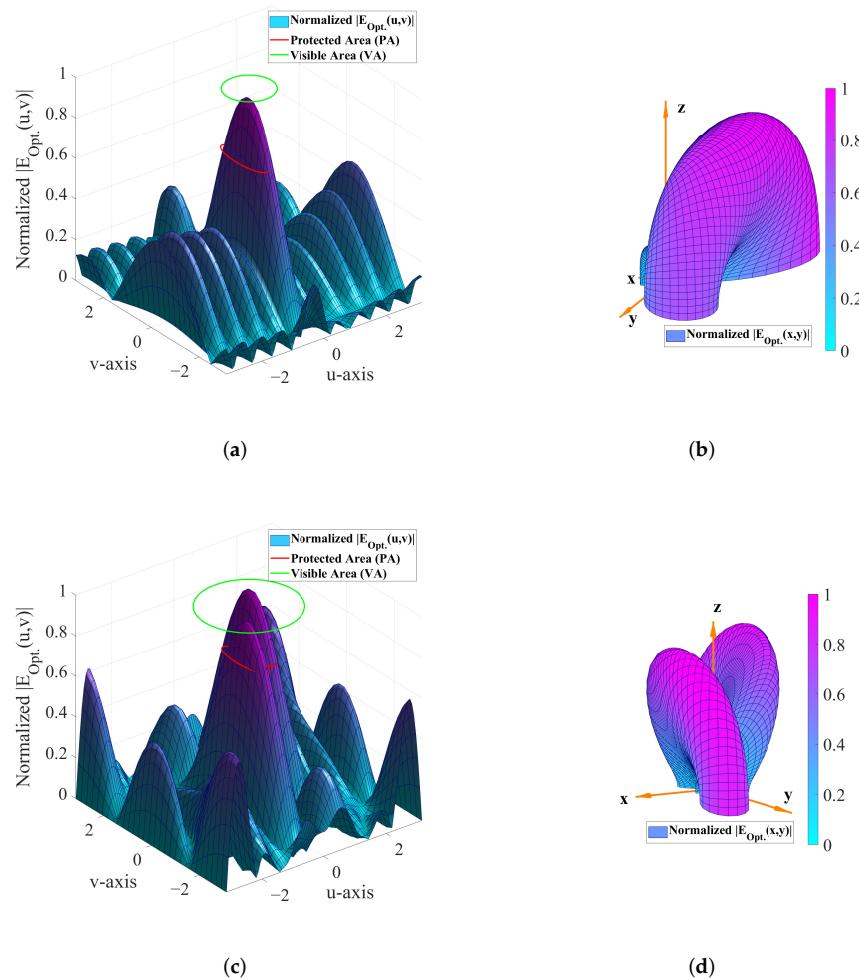

(**a**)

(**b**)

(**c**)

(**d**)

Figure 9. Regenerated optimized electric field patterns in the (u, v) space and in spherical coordinates, as produced by a 10×3 PMS. (**a**) Single-beam scenario in (u, v)-space. (**b**) Single-beam scenario in spherical coordinates. (**c**) Dual-beam scenario in (u, v)-space. (**d**) Dual-beam scenario in spherical coordinates.

Finally, Figure 10 shows the project pattern, the electric field pattern before optimization, and the electric field pattern after optimization in xz- and yz-planes depicted in polar coordinates. As is evident from Figure 10a–e, omitting the amplitude information produces suboptimal radiation patterns (pink dotted curves). However, by applying the proposed optimization strategy, the project patterns (black dashed curves) are recovered with a high precision (blue solid curves). From these examples, one can also notice that in single-beam scenarios with strong inclinations of the main beam, besides the main beam, there are parasitic sidelobes in the VA. These sidelobes are also present in the project pattern $F(u, v)$ and are due to the rather small aperture size and small number of elements in a 10×3 PMS.
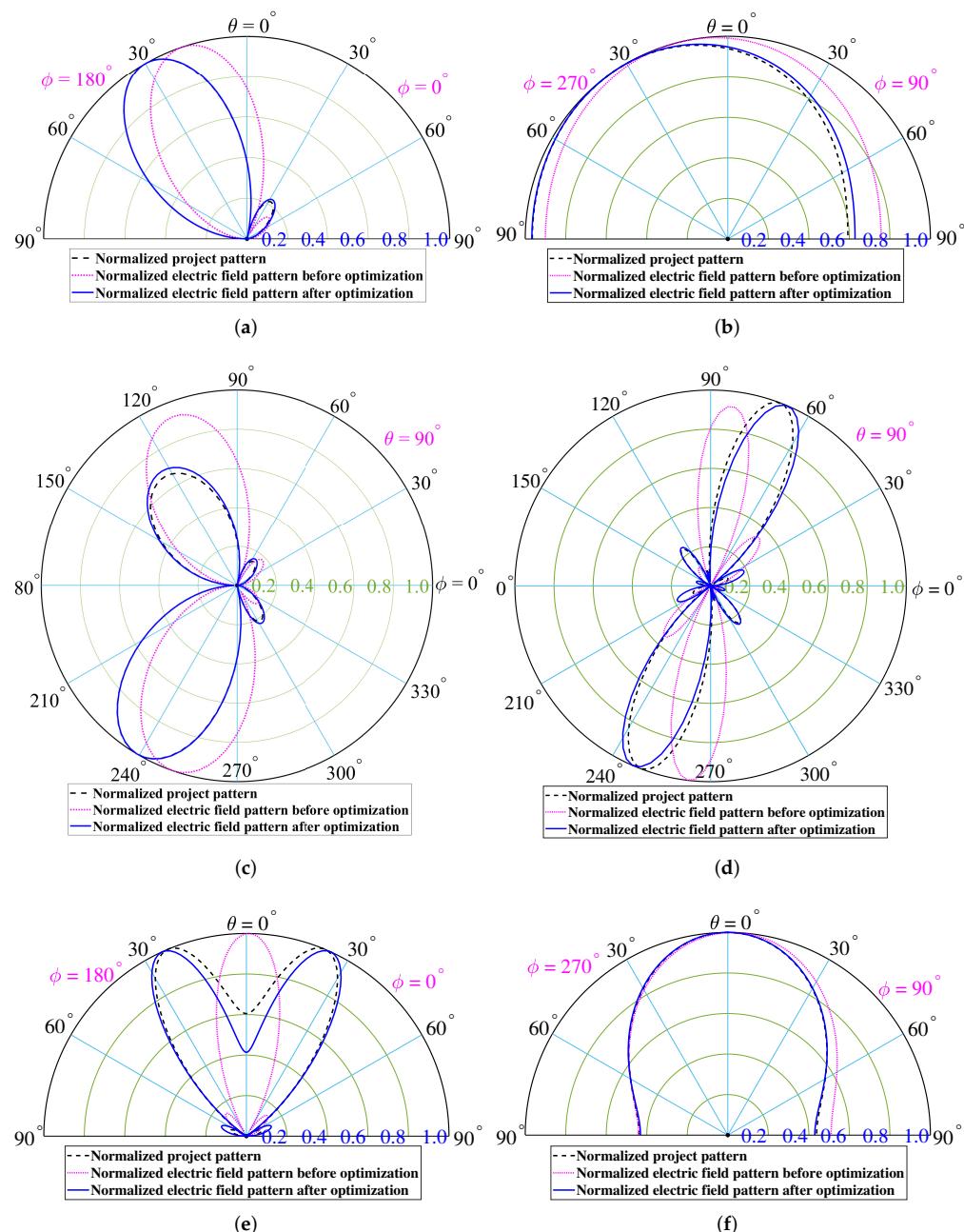
Figure 10. The project pattern and the electric field pattern before optimization, and the electric field pattern after optimization in polar coordinates for single- and dual-beam scenarios. (**a**) Single-beam scenario in polar coordinates, *xz*-plane. (**b**) Single-beam scenario in polar coordinates, *yz*-plane. (**c**) Single-beam scenario in polar coordinates, *xy*-plane. (**d**) Dual-beam scenario in polar coordinates, *xy*-plane. (**e**) Dual-beam scenario in polar coordinates, *xz*-plane. (**f**) Dual-beam scenario in polar coordinates, *yz*-plane.

5. Replacing Optimization Algorithms by Trained ANNs

Although aperture phase distributions can be recovered successfully by applying the optimization method discussed above, the optimization process is computationally expensive and slow. Therefore, it is unsuitable for applications that require real-time beamforming. However, the computational complexity can be dramatically reduced if instead one uses an FFNN pretrained on the optimal phase distributions obtained for a large set of beam deflections. In this way, the complex beamforming problem can be solved rapidly, even on moderate hardware. The pretrained FFNN in this case realizes a set of

nonlinear functions that relate the directions of the main beam (or several beams) to the required reflection phases on a PMS. When dealing with a PMS controlled by varactor diodes, another FFNN can be pretrained to deduce the varactor control voltages from the phase distribution produced by the first FFNN. The second FFNN may also perform additional functions, e.g., it may implement corrections to the control voltages that would take into account parasitic coupling between the PMS elements, etc.

In light of what has been just discussed, in this work we propose and develop two use cases for such pretrained ANNs: (1) a beamforming neural network (BFNN) and (2) a control FFNN. In the first case, i.e., the BFNN case, the phases are computed directly by a pretrained FFNN by inputting the desired main beam(s) targets into the model. In the second case, i.e., the control FFNN case, a pretrained FFNN takes the output of the BFNN as its input and computes the required control voltages. Figure 11a presents the proposed ANN configuration, in which the blocks inside a dashed blue rectangle represent the control FFNN. Note that we deliberately split the ANN configuration into two FFNNs trained separately, because this allows us to have a better control over the training process. Moreover, in this work, in order to reduce the number of necessary neurons in the control FFNN, we subdivide it into repeating equal sub-blocks (atan2(x, y) and CTRLNN) shown in the figure. Such subdivision is possible if the PMS cell control voltages are independent from each other. The function of each component can be separately verified.
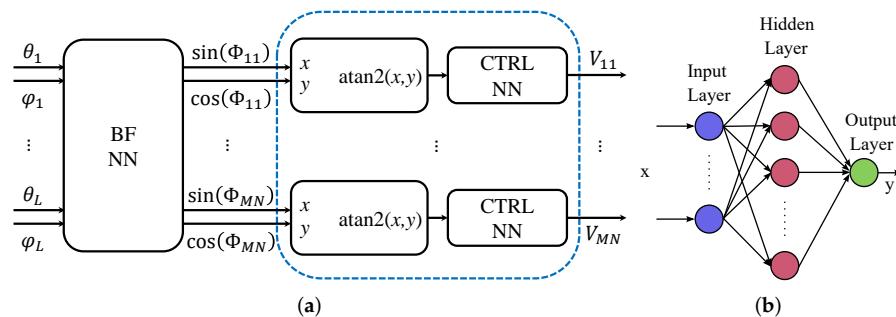

Figure 11. Block diagram and graphical representation of a Feed-Forward Neural Networks (FFNN) approach. (**a**) Connection of BFNN and control FFNN. (**b**) Internal structure of an FFNN.

In our realization, the BFNN consists of one input layer, one hidden layer with 32 neurons, and one output layer. A graphical representation of such FFNN is depicted in Figure 11b. The input layer of the BFNN has $2 \times L$ neurons to accept the parameters of the main beams for each possible radiation pattern realization. The output layer comprises $2 \times M \times N = 60$ neurons, which output the values of $\sin \Phi_{mn}$ and $\cos \Phi_{mn}$. The reason why such an approach was taken is explained in Section 5.1. The input parameters of the BFNN represented by vector $\vec{X}_{BFNN} = (\theta_1, \varphi_1, \ldots, \theta_L, \varphi_L)$ are the spherical angles that define the main beams' directions, and the output parameters denoted by $\vec{Y}_{BFNN} = (\sin \Phi_{11}, \cos \Phi_{11}, \ldots, \sin \Phi_{MN}, \cos \Phi_{MN})$ correspond to the reconstructed reflection phase values for each PMS cell. These are the data to which we fit the first FFNN model.

Each CTRLNN sub-block consists of one input neuron, one hidden layer with 20 neurons, and one output neuron. For CTRLNN sub-blocks, the PMS cell's reflection phase values are defined as the inputs, i.e., $X_{k,CTRLNN} = \text{atan2}(Y_{2k-1,BFNN}, Y_{2k,BFNN})$, where $k = 1, \ldots M \times N$, and the PMS cell controlling voltages are defined as the outputs: $Y_{(n-1)M+m,CTRLNN} = V_{mn}$. The atan2() sub-blocks realize the four-quadrant arctangent function. The CTRLNN model is fit to these data.

In the next two subsections, we give details on the training process of these two FFNNs.

5.1. Generating Datasets for BFNN Training for Single-Beam and Dual-Beam Cases

Datasets consisting of 3200 and 1000 data samples at 5 GHz and 10 GHz have been analyzed for single-beam and dual-beam cases using the PMS model shown in Figure 3, respectively. The datasets are generated so that the main beam directions (θ_i, φ_i), $i = 1, \ldots L$,

become the inputs of the training model and a vector of $M \times N$ reflection phase values is the output of the training model. We have taken 32 arbitrary beam directions distributed approximately equidistantly in the hemisphere $z > 0$ with at most $75°$ beam tilt angle to generate the datasets to train the BFNN. The generated datasets include 100 data points for each direction. Approximately 70% of the data are used to train the network, and the remaining 30% are utilized for validation. We have used 2240 and 700 samples to train the network in the single-beam and the dual-beam cases, respectively, and 960 and 300 samples were used for validation. Instead of using the phase values directly in the training process, we apply trigonometric sin and cos functions to the phases and use the resulting sine and cosine values in the training in order to mitigate the 2π phase jumps. This approach has proven to work better than any phase unwrapping. Regarding the volume of training data, it should be mentioned that, usually, the ratio between the number of samples and the number of features within each sample is more important than just the total number of samples; therefore, we consider the generated dataset volume to be sufficient for our purpose.

5.2. Generating Datasets for CTRLNN Training

For the CTRLNN sub-blocks, the training dataset was generated using the analytical model of a varactor-controlled PMS that we have developed in an earlier work of ours [29]. The structure of the PMS is depicted in Figure 12a. The unit cell is inside a dashed square in this figure. The unit cells are squares with the size of 6.8×6.8 mm^2. As compared to [28], the patch size w can be reduced from 3 mm to 1.3 mm to enable a higher operating frequency of 10 GHz. The independent units to which the control voltages are applied can be either single unit cells of the PMS or groups of unit cells. The figure also shows X- and Y-controlling lines to which pulsed control voltage can be applied. For more details on the control network layout and operation, the reader is referred to [29].
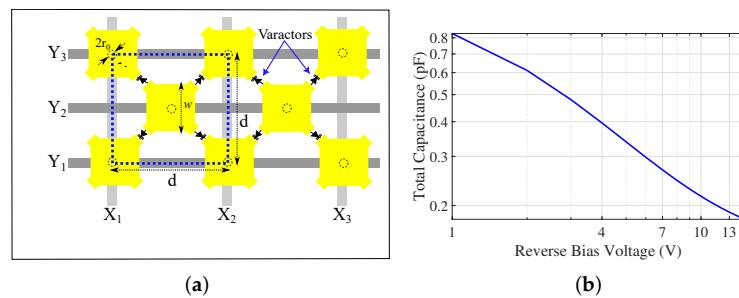

(a)	(b)

Figure 12. (**a**) Geometry of the PMS. The dashed square delimits a unit cell of the structure. The period of the structure $d = 6.8$ mm. The wire radius is $r_0 = 0.3$ mm and the patch width is $w = 3$ mm for a PMS operating at 5 GHz and $w = 1.3$ mm at 10 GHz. (**b**) Capacitance vs. voltage for the varactor diode model MA46H120 simulated in Agilent ADS.

The top layer of the PMS contains a chessboard-like array of square patches loaded with varactors at the patch corners. The layers with X- and Y-controlling lines and other elements (filtering and memory capacitors [29]) are located below. By analyzing this structure, we can relate the required reflection phases to the necessary input bias voltages applied to the varactors. Indeed, the bias voltage determines the varactor diode junction capacitance that in turn determines the resonant frequency of the cell and the local reflection phase [29]. We use these relations to generate the datasets for the CTRLNN.

The complex reflection coefficient at every unit cell is calculated using the analytical model developed in [29]. The diode junction capacitance varies with the applied reverse bias approximately as

$$C = C_0(V/\varphi_J + 1)^{-\gamma}, \tag{14}$$

where $C_0 = 1.09$ pF is the varactor diode capacitance at $V = 0$ V, and $\gamma = 0.68$ is the slope of the $\log C$ vs. $\log V$ curve (Figure 12b). The value of the built-in junction potential φ_J is

about 0.7 V for Si and 1.3 V for GaAs at room temperature. Figure 12b shows the junction capacitance as a function of bias voltage for the varactor diode used for modeling [29].

From Equation (14), the reverse voltage is

$$V = \left((C_0/C)^{1/\gamma} - 1 \right) \varphi_J. \tag{15}$$

The phase of complex electric field reflection coefficient can be computed as

$$\varphi = \angle R_s^{TM} = \angle \left(\frac{1 - Y_s^{TM} \cos \theta}{1 + Y_s^{TM} \cos \theta} \right), \tag{16}$$

where Y_s^{TM} is the normalized complex input admittance of the MS structure understood as a parallel connection of the surface admittance of the varactor-loaded patch grid and the input admittance of a wire medium slab [29].

For generating the datasets to train the CTRLNN sub-blocks, the reflection phases obtained by this analytical model are imported into the CTRLNN model as training inputs. The corresponding varactor bias voltages are the outputs of this training model. Like before, about 70% of the dataset is used to train the CTRLNN, and the remaining data are utilized for validation. The output neurons of the CTRLNN produce the values of bias voltages in the range from 1 to 9 V.

5.3. Performance of the BFNN for Single-Beam and Dual-Beam Cases

The FFNN model of BFNN runs on a HP Pavilion desktop computer (model no. TG01-1008np) with an Intel® Core™ i5-10400F CPU @ 2.90 GHz and 32 GB RAM. Training of the BFNN takes less than 20 min; however, the trained network can predict the necessary phase distribution for arbitrary beam directions in a fraction of second, which is much less time-consuming than the global optimization of the phase distribution in MATLAB that can take many hours to complete on the same hardware. Moreover, the BFNN model needs much less memory space as compared to the optimization code.

The correlation between the numerically optimized phase values and the values predicted by the trained BFNN in a single-beam scenario is quantified by the correlation coefficient, which was calculated to validate BFNN performance. These results are depicted in Figure 13. Figure 13a presents the correlation between the predicted phase values and the optimized values used for training the BFNN. As seen in Figure 13a, 87.5% of the predictions are above the accuracy average of the BFNN predictions, which reaches 0.98. As shown in Figure 13b, all of the predicted values for 30 different sets of (θ_i, φ_i) pairs from the validation set, which are not included in the dataset used for training, are predicted with more than 83% accuracy. However, the mean accuracy for predictions is decreased to 0.92 in this case, Figure 13b.

Finally, in Figure 14 we present results for the electric field patterns of 10×3 PMS obtained with the optimized FT-based beamforming method realized in MATLAB and predicted by the BFNN in single- and dual-beam scenarios with different direction(s) of the main beam(s). The considered beam directions are as follows: For the single-beam case, $(\theta_1, \varphi_1) = \{(30°, 45°), (60.2°, 221.1°), (70.23°, 63.46°)\}$ and for the dual-beam case, $(\theta_1, \varphi_1) = (30°, 45°)$ and $(\theta_2, \varphi_2) = (30°, 225°)$. In the single-beam case, the case with $(\theta_1, \varphi_1) = (30°, 45°)$ is one of the cases included in the training dataset, Figure 14a–c. However, the beam angles $(\theta_{24}, \varphi_{24}) = (60.2°, 221.1°)$ and $(\theta_{30}, \varphi_{30}) = (70.23°, 63.46°)$ are not in the training dataset and are just used for validating BFNN performance for arbitrary input data, Figure 14d–i, respectively. In the dual-beam case, the pairs $(\theta_1, \varphi_1) = (30°, 45°)$ and $(\theta_2, \varphi_2) = (30°, 225°)$ are included in the training dataset, Figure 14j–l. The results show a very good agreement between the numerically optimized and the BFNN-predicted data.
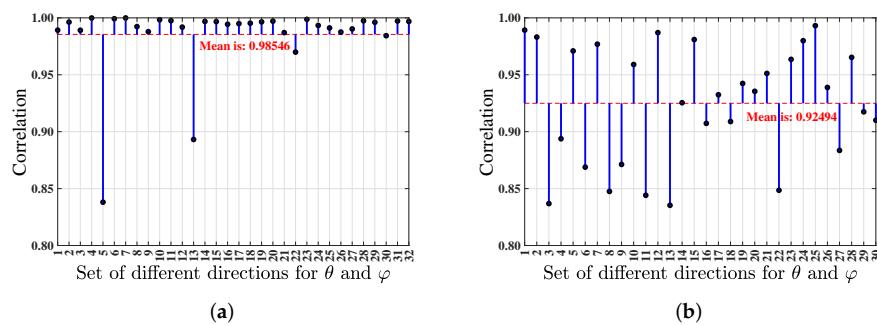
(**a**)

(**b**)

Figure 13. Correlation between the optimized and BFNN-estimated phase distributions for a 10×3 PMS in a single-beam scenario. (**a**) Correlation of predicted vs. optimized phases from the training dataset. (**b**) Correlation of predicted vs. optimized phases from the validation dataset.

5.4. Performance Validation of the CTRLNN

The CTRLNN was trained on the same computer as the BFNN. The typical training time is less than 10 min. After training, the CTRLNN model produces a result in a fraction of second. The ratio of 70%/15%/15% was selected for the training/validating/testing datasets, respectively. To validate the performance of the trained network, the mean square error (MSE) as a function of the epoch number was calculated and plotted in Figure 15a. It was found that the control voltage MSE is about 5.54×10^{-5} V^2 at epoch 655. In total, 1000 epochs were used as the maximum number of epochs in the training process.

Figure 15b plots the reflection phase versus the varactor bias voltage as obtained by simulations in Agilent ADS and predicted by the trained CTRLNN. As one can see, the results predicted by the CTRLNN match the simulated results very well.
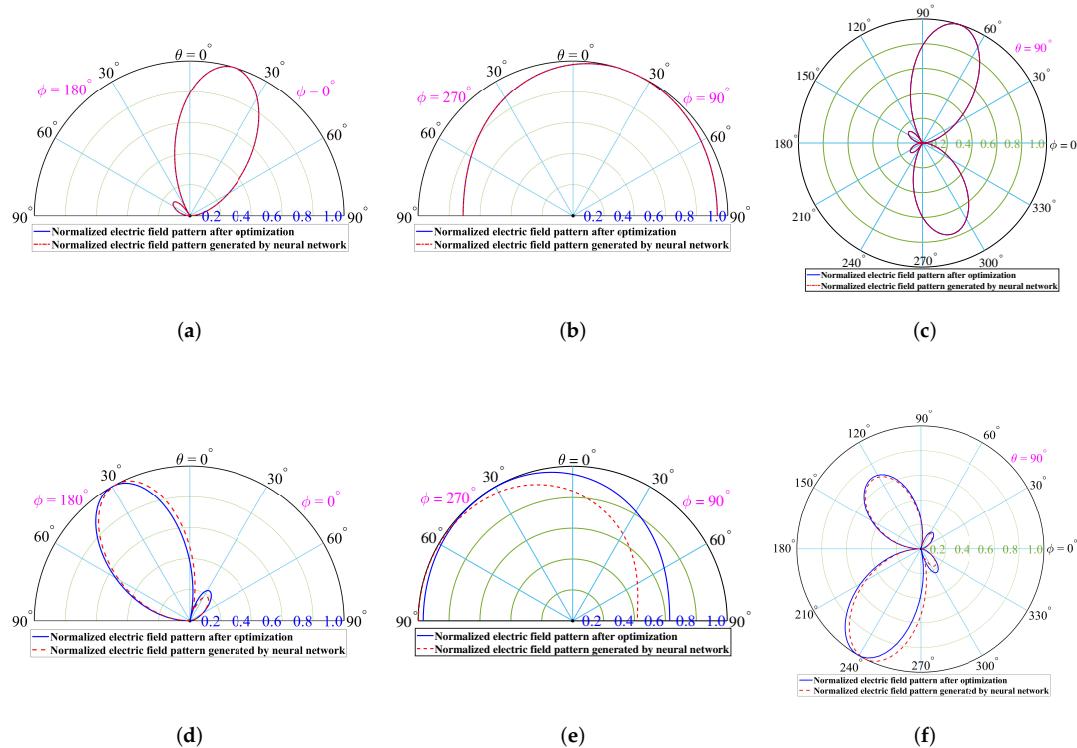

(**a**)

(**b**)

(**c**)

(**d**)

(**e**)

(**f**)

Figure 14. *Cont.*

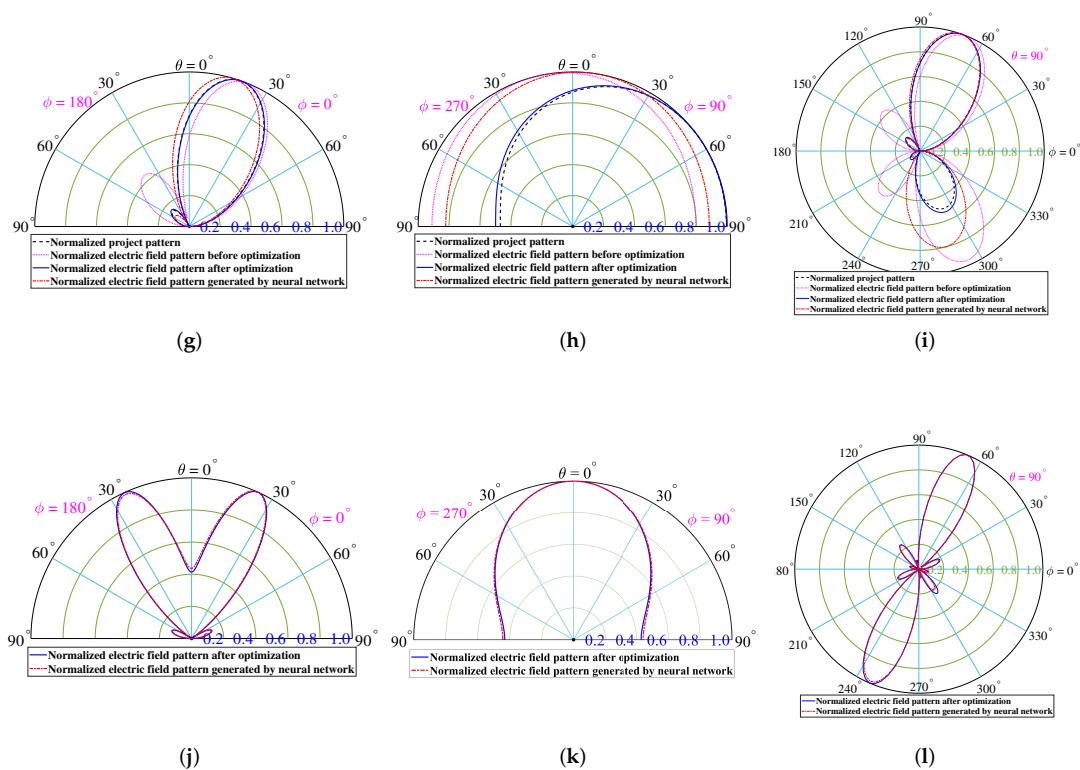**(g)**   **(h)**   **(i)**

(j)   **(k)**   **(l)**

Figure 14. The optimized electric field patterns and the ANN-predicted electric field patterns in polar coordinates, as produced by a 3 × 10 PMS. (**a**) Single-beam scenario in polar coordinates at 5 GHz, *xz*-plane. (**b**) Same scenario, *yz*-plane. (**c**) Same scenario, *xy*-plane. (**d**) Single-beam scenario in polar coordinates at 5 GHz, *xz*-plane. (**e**) Same scenario, *yz*-plane. (**f**) Same scenario, *xy*-plane. (**g**) Single-beam scenario in polar coordinates at 5 GHz, *xz*-plane. (**h**) Same scenario, *yz*-plane. (**i**) Same scenario, *xy*-plane. (**j**) Dual-beam scenario in polar coordinates at 10 GHz, *xz*-plane. (**k**) Same scenario, *yz*-plane. (**l**) Same scenario, *xy*-plane.
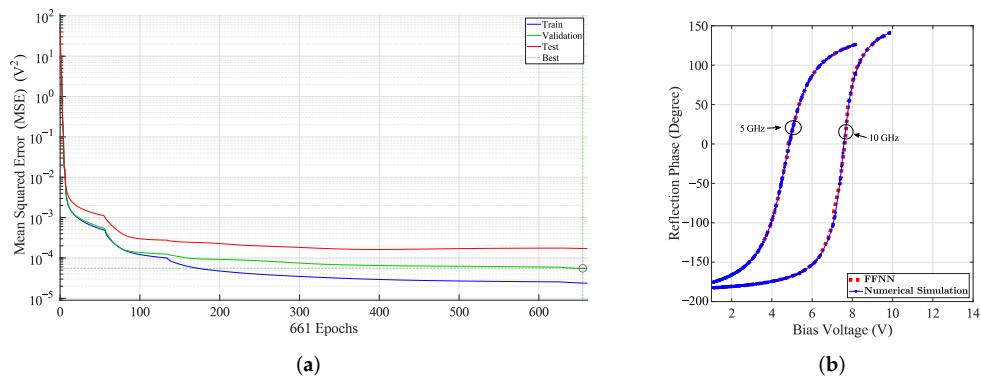

(a)   **(b)**

Figure 15. The corresponding MSE as a function of the epoch number and reflection phase versus applied bias voltage. (**a**) MSE as a function of the epoch number. (**b**) Reflection phase versus applied bias voltage.

6. Prototyping and Preliminary Experimental Results

In this section, we report preliminary experimental results obtained with a PMS prototype with 3 × 10 unit cells. The prototype was designed using the analytical–numerical model developed in [29]. To control direction of the reflected beam, the phase gradient along the PMS was generated by applying varying dc voltages to the varactors that belong to neighboring unit cells. The phase gradient is approximately proportional to the bias

voltage gradient. In this way, we achieved beam steering in the direction of the applied voltage gradient. A view of the prototype PMS installed in a plastic holder is shown in Figure 16a.
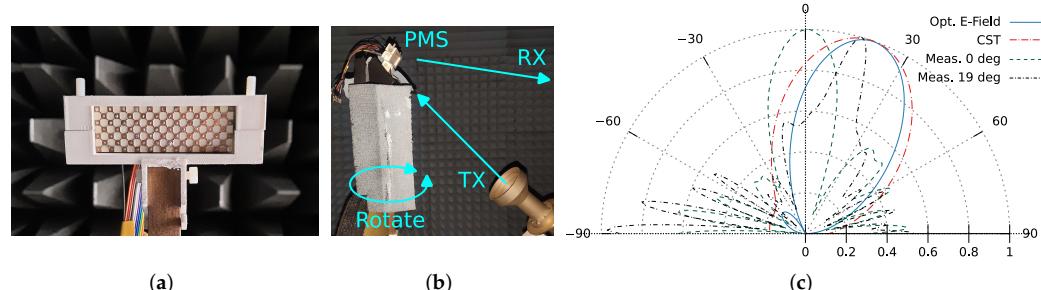

(a) (b) (c)

Figure 16. PMS prototype and results of radiation pattern measurements and simulations. (**a**) The PMS installed in a custom 3D-printed plastic holder. (**b**) The experimental setup. (**c**) Radiation patterns in the *xz*-plane produced by 3×10 PMS.

The PMS radiation pattern measurements were performed using the anechoic chamber facilities of the Department of Electronics, Telecommunications and Informatics of University of Aveiro. The measurement setup is shown in Figure 16b. In the experimental setup, the TX antenna (a circular horn) and the PMS prototype are fixed on the same rotating support so that the incidence is always close to normal. The incident wave is linearly polarized with the electric field vector parallel to the elongated side of the PMS. The RX antenna (a Vivaldi antenna, not seen in the figure) is fixed and is placed a few meters away from the rotating support. When the support rotates, the RX antenna measures the signal scattered by the PMS sample at varying angles.

Figure 16c depicts the results of the radiation pattern measurements in the *xz*-plane ($\theta = 0°$ corresponds to the normal to the PMS) alongside the results of the analytical beamforming model and full-wave simulations in SIMULIA CST Studio Suite, for the cases with and without the bias voltage. The applied voltage gradient corresponds to the reflection phase variation from $-50°$ to $50°$ (varactors' capacitance values vary from 0.25 to 0.2 pF) in the direction of the long side of the PMS, which should produce the main beam pointing at $(\theta_0, \varphi_0) \approx (19°, 0°)$.

As can be seen in this figure, the maximum of the PMS radiation pattern without the applied voltage points at $\theta_0 \approx 0°$, as expected (green dashed curve). When the voltage gradient is applied, the maximum of the radiation pattern shifts to $\theta_0 \approx 17°$ (black dash-dotted curve). The radiation pattern generated using the beamforming methodology developed in this article (blue solid curve with a maximum at $\theta = 19°$) and the result of full-wave simulations in SIMULIA CST Studio Suite (red dash-dotted curve with the maximum at $\theta_0 \approx 18°$) are also depicted in the same figure.

We may conclude that beam inclinations in all these cases are in good agreement. However, the beam shape of the prototype PMS is distorted, and sidelobes with relatively high amplitude are clearly visible. We have investigated possible reasons of such effects and concluded that they were caused by scattering of the TX antenna field by the elements of the experimental setup other than the PMS itself. When such parasitic scattered field is added to the field reflected by the PMS, a distorted radiation pattern is observed due to the interference between the two fields. Therefore, it was concluded that a more elaborate experimental setup is needed in order to test more complex beamforming scenarios. In particular, a larger PMS sample may be needed to increase measurement accuracy. Fabrication of such sample and additional measurements are reserved for a future work.

For more details on the related experimental and analytical methods, the reader is referred to Refs. [28,29,46].

7. Discussion of the Results

In this section we discuss the limitations of our study and also compare our beamforming PMS design to the other designs known in the literature.

7.1. Beamforming Methodology Limitations

The optimization methodology that we propose in this work was implemented using interpreted MATLAB scripts. Moreover, in order to have a visual feedback, a real-time indication of the optimization convergence through MATLAB's Integrated Development Environment (IDE) was used. Because of this, the numerical optimization was quite time-consuming, which forced us to consider only a limited subset of possible beamforming scenarios. Porting the developed code to platforms such as C++ can potentially speed up the algorithm by orders of magnitude and shall give us an opportunity to study PMS with larger dimensions, which is reserved for a future work.

The main limitations in the presented beamforming results are related to the moderate number of the controllable elements in the PMS and the relatively small size of the PMS. Indeed, the considered PMS only has $3 \times 10 = 30$ unit cells, which allows for a rather restrained set of beamforming scenarios. There are two reasons to keep the unit cell count low: (1) feasibility of the initial prototype implementation and (2) reduction of the computation time during phase distribution optimizations with MATLAB scripts. However, even with such a limited PMS we have realized a number of single- and dual-beam beamforming scenarios. We have also trained the BFNN and the CTRLNN networks on the generated datasets and confirmed that the proposed beamforming approach is feasible.

To generate beamforming datasets for the prototype structure with 30 unit cells, 32 approximately equidistant directions have been selected in the frontal PMS hemisphere. In fact, the number of such assumed beam directions as well as the number of PMS unit cells limits the achievable beamforming accuracy. Therefore, by increasing the number of unit cells and the number of predetermined beam directions, more elaborate beamforming scenarios can be realized.

7.2. Pros and Cons of the PMS Design

In addition to the above, a beam steering scenario was experimentally tested with a prototype of an electrically controllable PMS studied in our previous works [28,29,46]. Although our beamforming methodology is applicable to a wide class of reactive MS structures that are able to control reflection phase, we decided to focus our attention on the passive varactor-loaded PMS with capacitive memory proposed in [29]. When compared to other realizations, such a PMS has certain advantages. In order to illustrate it, we have compiled a comparison table (Table 1).

The items in this table are sorted into three groups organized by the complexity class criterion, which is defined based on the set of features that are present in a design:

- Class I: Passive structures without dc feed or with just (pulsed) control voltage(s) and with a small number of passive components per unit cell and a relatively simple layout;
- Class II: Active structures with dc feed and control voltage, with a moderate number of components (both active and passive) and with a moderate layout complexity;
- Class III: Active structures with a dc feed, high number of components, and a complex layout.

As can be seen from this table, our design belongs to Class I, due to the fact that it is fully passive and does not require any dc feed, has a small number of passive components per unit cell, and is controlled with pulsed voltage. The designs that belong to Class II are more complex, as they need more components per unit cell. They also incorporate active devices (e.g., flip-flops, shift registers, etc.) that constantly consume dc power. Finally, Class III is for even more elaborate designs that require continuous dc feed and a significant number of active components assembled in a circuit with complex topology.

Although the increased complexity of the designs that fall into Classes II and III typically brings new functionalities, the devices that belong to Class I are best in terms of energy efficiency. They also use a small number of passive components per unit cell, which

simplifies fabrication and reduces cost. Unfortunately, not all of them are electronically controllable. Among the designs that belong to Class I, our design has an extra advantage of reconfigurability. Moreover, although being passive, it is able to keep its configuration state for some time between sequential reprogramming. For more details, the reader is referred to [29].

Table 1. Comparison of different beamforming MS designs [†].

Ref.	Frequency [GHz]	Compon. [1] per Cell	Type	Beam Number	Tunable	R.S. [2]	C.C. [3]
This Work	5 & 10	4 Var. [4]	Analog	1/2/M.B. [5]	Yes	Yes	Class I
[52]	10	–	–	1	No	No	Class I
[53]	8–20	–	Mech. [6]	1	Yes	Yes	Class I
[54]	10–12	1 PIN Diode	Digital (1-bit)	1/2/4	Yes	No	Class I
[55]	5.8	2 Var.	Analog	1	Yes	Yes	Class II
[27]	8–15	1 Bias Diode	Digital (1/2-bit)	1/2/4	Yes	Yes	Class II
[56]	9.5	2 PIN Diodes	Digital (2-bit)	2	Yes	Yes	Class II
[57]	3	SPDT [7]	Digital (1-bit)	M.P. [8]	Yes	Yes	Class II
[58]	8	2 PIN Diodes	Analog & Digital	M.B.	Yes	Yes	Class II
[59]	28	1 PIN Diode	Digital (1-bit)	1	Yes	Yes	Class III
[60]	5.8	1 DFF [9] & SR [10] & Dec. [11]	Digital (1-bit)	M.B.	Yes	Yes	Class III

[1] Component; [2] Remembers State; [3] Complexity Class; [4] Varactor; [5] Multi-Beam; [6] Mechanical; [7] Single-Pole-Double-Throw switch chip; [8] Multi-Purpose; [9] D Flip-Flop; [10] Shift Register; [11] Decoder. [†] Under no circumstances this table should be considered as a complete list of representative works; it is only a selection based on our own preferences and limited knowledge.

8. Conclusions

An inverse design method has been introduced, which combines FT-based beamforming, numerical optimization, and machine learning techniques. In our method, first, the aperture field distribution is obtained by applying Fourier transform to the desired far-field radiation pattern. Then, the aperture field amplitude information is discarded; however, the phase information is retained and is used as an input to the developed optimization algorithm that further improves beamforming accuracy. Next, this optimizing FT-based beamforming method is used to generate datasets of required aperture phase distributions vs. a number of single- and double-beam scenarios. The generated datasets are used to train a Beamforming Feed-forward Neural Network (BFNN), which is able to generate the necessary phase distribution data in a fraction of second.

Moreover, to provide control of the PMS and generate the necessary controlling voltages for the unit cells of the PMS, we have proposed to use another trained Control Neural Network (CTRLNN), which, in practical applications, can also perform additional functions, such as compensating for the unit cell coupling in the PMS, etc. By employing the developed approach, the required phase distribution over the PMS and, consequently, the required bias voltages to control the PMS unit cells are calculated in real-time. The BFNN and CTRLNN networks have been trained on the generated datasets for a number of beamforming scenarios. The performance of the neural networks has been validated. The correlation between the BFNN output and the results of the optimizing FT-based beamforming method reaches 98% in the best cases, and is generally above 90% in other cases. The validated CTRLNN performance is also high, with the control voltage MSE below 10^{-4} V^2.

Overall, we have observed that the desired radiation patterns are recovered with high precision when either the optimizing FT-based method or the trained ANNs are used, despite ignoring the magnitude information at the Fourier transform stage. However, at high inclination angles, parasitic sidelobes may appear in the reconstructed patterns, a

phenomenon that is related to the rather small number of unit cell rows and columns in the PMS sample on which the study was performed.

Author Contributions: Conceptualization, S.M.; methodology, S.M., K.K. and A.A.; software, K.K. and A.A.; validation, K.K., A.A. and S.M.; formal analysis, S.M., K.K. and A.A.; investigation, K.K. and A.A.; resources, S.M.; data curation, K.K. and A.A.; writing—original draft preparation, K.K., A.A. and S.M.; writing—review and editing, S.M., K.K. and A.A.; visualization, K.K. and A.A; supervision, S.M.; project administration, S.M.; funding acquisition, S.M. All authors have read and agreed to the published version of the manuscript.

Data Availability Statement: The programs that generate the data presented in this study are openly available at https://github.com/KeivanKaboutari/AI-Beamforming (accessed on 13 March 2024).

Conflicts of Interest: The authors declare no conflicts of interest.

References

1. Malviya, L.; Panigrahi, R.; Kartikeyan, M. *MIMO Antennas for Wireless Communication: Theory and Design*, 1st ed.; CRC Press: Boca Raton, FL, USA, 2020. [CrossRef]
2. Hussain, R.; Sharawi, M.S. 5G MIMO Antenna Designs for Base Station and User Equipment: Some recent developments and trends. *IEEE Antennas Propag. Mag.* **2022**, *64*, 95–107. [CrossRef]
3. Raj, T.; Mishra, R.; Kumar, P.; Kapoor, A. Advances in MIMO Antenna Design for 5G: A Comprehensive Review. *Sensors* **2023**, *23*, 6329. [CrossRef] [PubMed]
4. Vadlamudi, R.; Dhamodharan, S. Nature enthused high isolation high gain miniaturized multiple-input multiple-output antenna for A-LTE/5G macro cell base transceiver station applications. *Int. J. Microw.-Comput.-Aided Eng.* **2021**, *31*, e22885. [CrossRef]
5. Farahat, A.E.; Hussein, K.F.A. Dual-Band (28/38 GHz) Wideband MIMO Antenna for 5G Mobile Applications. *IEEE Access* **2022**, *10*, 32213–32223. [CrossRef]
6. Kaboutari, K.; Pinho, P.; Oliveira, A. 5G Indoor Micro-BTS Antenna Design Using Quad-MIMO MED Antennas. In Proceedings of the 2023 Photonics & Electromagnetics Research Symposium (PIERS), Prague, Czech Republic, 3–6 July 2023; pp. 814–822. [CrossRef]
7. Navarro, A.; Mostardinha, P.; Varum, T.; Matos, J.; Maslovski, S. Double-dielectric microstrip ultrahigh-frequency antenna for digital terrestrial television. *Appl. Sci.* **2020**, *10*, 8640. [CrossRef]
8. Teimouri, M.; Ghobadi, C.; Nourinia, J.; Kaboutari, K.; Shokri, M.; Virdee, B. Broadband Printed Dipole Antenna with Integrated Balun and Tuning Element for DTV Application. *AEU-Int. J. Electron. Commun.* **2022**, *148*, 154161. [CrossRef]
9. Abraray, A.; Fernandes, R.T.; Maslovski, S.I. Design and optimization of compact array rectennas for harvesting wireless power. In Proceedings of the IET Conference Publications, Nanjing, China, 12–13 October 2018; Volume 2018, pp. 2–5. [CrossRef]
10. Khorasani, S.; Nourinia, J.; Ghobadi, C.; Shokri, M.; Hatamian, A.; Virdee, B. Dual-band magneto-electric dipole antenna with high-gain for base-station applications. *AEU-Int. J. Electron. Commun.* **2021**, *134*, 153696. [CrossRef]
11. Kaboutari, K.; Zabihi, A.; Virdee, B.; Salmasi, M. Microstrip patch antenna array with cosecant-squared radiation pattern profile. *AEU-Int. J. Electron. Commun.* **2019**, *106*, 82–88. [CrossRef]
12. Kaboutari, K.; Hosseini, V. A compact 4-element printed planar MIMO antenna system with isolation enhancement for ISM band operation. *AEU-Int. J. Electron. Commun.* **2021**, *134*, 153687. [CrossRef]
13. Kaboutari, K.; Pinho, P.; Maslovski, S. Beamforming Antenna Arrays and Metasurfaces for Medical Imaging: From Overview to Suggesting a new Imaging Modality. In Proceedings of the 2021 Photonics Electromagnetics Research Symposium (PIERS), Hangzhou, China, 21–25 November 2021; pp. 1942–1951. [CrossRef]
14. Shokri, M.; Ghobadi, C.; Nourinia, J.; Pinho, P.; Amiri, Z.; Barzegari, R.; Siahcheshm, A.; Shapour, F.; Kaboutari, K. A Compact Four Elements Self-Isolated MIMO Antenna for C-Band Applications. In Proceedings of the 2023 IEEE 27th Workshop on Signal and Power Integrity (SPI), Aveiro, Portugal, 7–10 May 2023; pp. 1–4. [CrossRef]
15. Butler, J. Beam-forming matrix simplifies design of electronically scanned antennas. *Electron. Des.* **1961**, *9*, 170–173.
16. Josefsson, L.; Persson, P. *Conformal Array Antenna Theory and Design*; Wiley-IEEE Press: Hoboken, NJ, USA, 2006; p. 370.
17. Blass, J. Multidirectional antenna—A new approach to stacked beams. In Proceedings of the 1958 IRE International Convention Record, New York, NY, USA, 1960; Volume 8, pp. 48–50. [CrossRef]

18. Lipsky, S. *Microwave Passive Direction Finding*; SciTech Publishing, Raleigh, USA, 2004; pp. 130–131.

19. Heba, S.; Heba, A.; Mustafa, M.; Amr, H. New distributed beamforming techniques based on optimized elliptical arc geometry for back lobe cancellation of linear antenna arrays. *Alex. Eng. J.* **2022**, *61*, 4623–4645. [CrossRef]

20. Sun, M.; Lv, Y.; Qian, J.; Kong, F.; Bai, X. Spatially Adaptive Beamforming Based on Time-Modulated Programmable Metasurface. In Proceedings of the 2023 International Applied Computational Electromagnetics Society Symposium (ACES-China), Hangzhou, China, 15–18 August 2023; pp. 1–2. [CrossRef]

21. Yoo, I.; Smith, D.R. Sub-6-GHz Uplink Massive MIMO System Using Holographic Beamforming Metasurfaces: A Conceptual Development. *IEEE Wirel. Commun. Lett.* **2023**, *12*, 644–648. [CrossRef]

22. Kimaryo, S.F.; Lee, K. Downlink Beamforming for Dynamic Metasurface Antennas. *IEEE Trans. Wirel. Commun.* **2023**, *22*, 4745–4755. [CrossRef]

23. Li, Y.; Long, X.; Oliveira, L.G.d.; Eisenbeis, J.; Alabd, M.B.; Bettinga, S.; Wan, X.; Cui, T.J.; Zwick, T. Programmable Metasurface Hybrid MIMO Beamforming: Channel Estimation, Data Transmission, and System Implementations at 28 GHz. *IEEE Syst. J.* **2023**, *17*, 1270–1281. [CrossRef]

24. Yang, F.; Yankai, M.; Yikai, C.; Shiwei, Q.; Shiwen, Y. A Novel Method for Maximum Directivity Synthesis of Irregular Phased Arrays. *IEEE Trans. Antennas Propag.* **2022**, *70*, pp. 4426–4438. [CrossRef]

25. Alhamed, A.; Kazan, O.; Gultepe, G.; Rebeiz, G. A Multiband/Multistandard 15-57 GHz Receive Phased-Array Module Based on 4 x 1 Beamformer IC and Supporting 5G NR FR2 Operation. *IEEE Trans. Microw. Theory Tech.* **2022**, *70*, 1732–1744. [CrossRef]

26. Hong, W.; Jiang, Z.; He, S.; Zhou, J.; Chen, P.; Yu, Z.; Chen, J.; Tian, L.; Yu, C.; Zhai, J.; et al. Limitations of phased arrays for 5G wireless communications. In Proceedings of the 2017 IEEE International Symposium on Antennas and Propagation USNC/URSI National Radio Science Meeting, San Diego, CA, USA, 9–14 July 2017; pp. 1467–1468. [CrossRef]

27. Cui, T.; Qi, M.; Wan, X.; Zhao, J.; Cheng, Q. Coding metamaterials, digital metamaterials and programmable metamaterials. *Light Sci. Appl.* **2014**, *3*, e218. [CrossRef]

28. Maslovski, S.; Abraray, A.; Kaboutari, K.; Nunes, D.; Navarro, A. Analytical and Numerical Modeling of Reconfigurable Beamforming Metasurfaces. In Proceedings of the 2021 Photonics Electromagnetics Research Symposium (PIERS), Hangzhou, China, 21–25 November 2021; pp. 2637–2647. [CrossRef]

29. Abraray, A.; Diogo, N.; Maslovski, S. Analytical and numerical modeling of reconfigurable reflecting metasurfaces with capacitive memory. *New J. Phys.* **2022**, *24*, 075003. [CrossRef]

30. Sejan, M.A.S.; Rahman, M.H.; Shin, B.S.; Oh, J.H.; You, Y.H.; Song, H.K. Machine Learning for Intelligent-Reflecting-Surface-Based Wireless Communication towards 6G: A Review. *Sensors* **2022**, *22*, 5405. [CrossRef]

31. Renzo, M.; Debbah, M.; Phan-Huy, D.; Zappone, A.; Alouini, M.; Yuen, C.; Sciancalepore, V.; Alexandropoulos, G.; Hoydis, J.; Gacanin, H.; et al. Smart radio environments empowered by reconfigurable AI meta-surfaces: An idea whose time has come. *J. Wireless Com. Network* **2019**, *2019*, 129. [CrossRef]

32. Pfeiffer, C.; Grbic, A. Metamaterial Huygens' Surfaces: Tailoring Wave Fronts with Reflectionless Sheets. *Phys. Rev. Lett.* **2013**, *110*, 197401. [CrossRef] [PubMed]

33. Kim, M.; Wong, A.; Eleftheriades, G. Optical Huygens' Metasurfaces with Independent Control of the Magnitude and Phase of the Local Reflection Coefficients. *Phys. Rev. X* **2014**, *4*, 041042. [CrossRef]

34. Epstein, A.; Eleftheriades, G. Synthesis of Passive Lossless Metasurfaces Using Auxiliary Fields for Reflectionless Beam Splitting and Perfect Reflection. *Phys. Rev. Letter* **2016**, *117*, 256103. [CrossRef] [PubMed]

35. Kwon, D.; Tretyakov, S. Perfect reflection control for impenetrable surfaces using surface waves of orthogonal polarization. *Phys. Rev. B* **2017**, *96*, 085438. [CrossRef]

36. Kwon, D. Lossless Scalar Metasurfaces for Anomalous Reflection Based on Efficient Surface Field Optimization. *IEEE Antennas Wirel. Propag. Lett.* **2018**, *17*, 1149–1152. [CrossRef]

37. Díaz-Rubio, A.; Asadchy, V.; Elsakka, A.; Tretyakov, S. From the generalized reflection law to the realization of perfect anomalous reflectors. *Sci. Adv.* **2017**, *3*, e16027142. [CrossRef] [PubMed]

38. Budhu, J.; Grbic, A. Passive Reflective Metasurfaces for Far-Field Beamforming. In Proceedings of the 2021 15th European Conference on Antennas and Propagation (EuCAP), Dusseldorf, Germany, 22–26 March 2021; pp. 1–4. [CrossRef]

39. Budhu, J.; Grbic, A. Perfectly Reflecting Metasurface Reflectarrays: Mutual Coupling Modeling Between Unique Elements Through Homogenization. *IEEE Trans. Antennas Propag.* **2021**, *69*, 122–134. [CrossRef]

40. Abraray, A.; Baghel, A.; Maslovski, S. Design of resonant metasurface absorber using feed-forward neural network. *Microw. Opt. Technol. Lett.* **2024**, *66*, e33977. [CrossRef]

41. Ross, C.; Gradoni, G.; Lim, Q.J.; Peng, Z. Engineering Reflective Metasurfaces With Ising Hamiltonian and Quantum Annealing. *IEEE Trans. Antennas Propag.* **2022**, *70*, 2841–2854. [CrossRef]

42. Li, R.; Cheng, J.; Dong, X.; Chang, S. Neural network aided diffractive metagratings for efficient beam splitting at terahertz frequencies. *J. Phys. D Appl. Phys.* **2022**, *55*, 155106. [CrossRef]

43. Maslovski, S.; Abraray, A.; Carvalho, N.; Navarro, A. Beamforming with Neural-Networked Programmable Metasurfaces. In Proceedings of the 2020 Fourteenth International Congress on Artificial Materials for Novel Wave Phenomena (Metamaterials), New York, NY, USA, 28 September–2 October 2020; pp. 225–227. [CrossRef]

44. Abraray, A.; Navarro, A.; Carvalho, N.; Maslovski, S. Towards Smart Beamforming Utilizing Neural- Networked Programmable Metasurfaces. In Proceedings of the 2021 Telecoms Conference (ConfTELE), Leiria, Portugal, 11–12 February 2021; pp. 1–6. [CrossRef]

45. Kaboutari, K.; Abraray, A.; Maslovski, S. Beamforming with Intelligent Metasurfaces: Operating Principles and Possible Implementations. In Proceedings of the 2021 International Conference on Electrical Engineering and Photonics (EExPolytech), Saint Petersburg, Russia, 14–15 October 2021; pp. 63–66. [CrossRef]

46. Abraray, A.; Pereira, R.; Kaboutari, K.; Maslovski, S. Realization of Programmable Chessboard Mushroom-type Metasurface for Beamforming Applications. In Proceedings of the 2023 Photonics & Electromagnetics Research Symposium (PIERS), Prague, Czech Republic, 3–6 July 2023; pp. 1909–1913. [CrossRef]

47. Gros, J.; Popov, V.; Odit, M.; Lenets, V.; Lerosey, G. A Reconfigurable Intelligent Surface at mmWave Based on a Binary Phase Tunable Metasurface. *IEEE Open J. Commun. Soc.* **2021**, *2*, 1055–1064. [CrossRef]

48. Taravati, S.; Eleftheriades, G. Programmable nonreciprocal meta-prism. *Sci. Rep.* **2021**, *11*, 7377. [CrossRef] [PubMed]

49. Byrd, R.; Gilbert, J.; Nocedal, J. A Trust Region Method Based on Interior Point Techniques for Nonlinear Programming. *Math. Program.* **2000**, *89*, 149–185. [CrossRef]

50. Audet, C.; Dennis, J. Analysis of Generalized Pattern Searches. *Siam J. Optim.* **2003**, *13*, 889–903. [CrossRef]

51. Waltz, R.; Morales, J.; Nocedal, J.; Orban, D. An interior algorithm for nonlinear optimization that combines line search and trust region steps. *Math. Program.* **2006**, *107*, 391–408. [CrossRef]

52. Budhu, J.; Szymanski, L.; Grbic, A. Design of Planar and Conformal, Passive, Lossless Metasurfaces That Beamform. *IEEE J. Microwaves* **2022**, *2*, 401–418. [CrossRef]

53. Wang, H.; Sui, S.; Li, Y.; Chen, H.; Wang, J.; Zhang, Z.; Qu, S. Passive reconfigurable coding metasurface for broadband manipulation of reflective amplitude, phase and polarization states. *Smart Mater. Struct.* **2019**, *29*, 015029. [CrossRef]

54. Gao, L.; Zhou, Y.; Zhu, H.; Zheng, P.; Liu, J.; He, Z.; Xu, Z.; Cui, Y. Reconfigurable Amplitude-Phase-Coding Metasurface with Flexible Beamforming Capability. *Electronics* **2023**, *12*, 4565. [CrossRef]

55. Pei, X.; Yin, H.; Tan, L.; Cao, L.; Li, Z.; Wang, K.; Zhang, K.; Björnson, E. RIS-Aided Wireless Communications: Prototyping, Adaptive Beamforming, and Indoor/Outdoor Field Trials. *IEEE Trans. Commun.* **2021**, *69*, 8627–8640. [CrossRef]

56. Zhang, L.; Chen, M.; Tang, W.; Dai, J.; Miao, L.; Zhou, X.; Jin, S.; Cheng, Q.; Cui, T. A wireless communication scheme based on space- and frequency-division multiplexing using digital metasurfaces. *Nat. Electron.* **2021**, *4*, 218—227. [CrossRef]

57. Wang, Z.X.; Shen, C.K.; Wu, J.W.; Xu, H.; Cheng, Q.; Ye, T.T.; Cui, T.J. A Long-Range and Nearly Passive RFID-Controlled Information Metasurface. *Adv. Opt. Mater.* **2024**, *12*, 2203114. [CrossRef]

58. Liao, J.; Guo, S.; Yuan, L.; Ji, C.; Huang, C.; Luo, X. Independent Manipulation of Reflection Amplitude and Phase by a Single-Layer Reconfigurable Metasurface. *Adv. Opt. Mater.* **2022**, *10*, 2101551. [CrossRef]

59. Wan, X.; Xiao, Q.; Zhang, Y.Z.; Li, Y.; Eisenbeis, J.; Wang, J.W.; Huang, Z.A.; Liu, H.X.; Zwick, T.; Cui, T.J. Reconfigurable Sum and Difference Beams Based on a Binary Programmable Metasurface. *IEEE Antennas Wirel. Propag. Lett.* **2021**, *20*, 381–385. [CrossRef]

60. Amri, M.M.; Tran, N.M.; Choi, K.W. Reconfigurable Intelligent Surface-Aided Wireless Communications: Adaptive Beamforming and Experimental Validations. *IEEE Access* **2021**, *9*, 147442–147457. [CrossRef]